Quantum Monte Carlo simulations of selected ammonia clusters (n = 2–5): Isotope effects on the ground state of typical hydrogen bonded systems

E. Curotto and Massimo Mella

Re-register for Table of Content Alerts

Create a profile.   Sign up today!

Quantum Monte Carlo simulations of selected ammonia clusters ($n = 2$–5): Isotope effects on the ground state of typical hydrogen bonded systems

E. Curotto[1,a)] and Massimo Mella[2,b)]

[1]*Department of Chemistry and Physics, Arcadia University, Glenside, Pennsylvania 19038-3295, USA*
[2]*School of Chemistry, Cardiff University, Cardiff CF10 3AT, United Kingdom*

Variational Monte Carlo, diffusion Monte Carlo, and stereographic projection path integral simulations are performed on eight selected species from the $(NH_3)_n$, $(ND_3)_n$, $(NH_2D)_n$, and $(NH_3)_{n-1}(ND_3)$ clusters. Each monomer is treated as a rigid body with the rotation spaces mapped by the stereographic projection coordinates. We compare the energy obtained from path integral simulations at several low temperatures with those obtained by diffusion Monte Carlo, for two dimers, and we find that at 4 K, the fully deuterated dimer energy is in excellent agreement with the ground state energy of the same. The ground state wavefunction for the $(NH_3)_{2-5}$ clusters is predominantly localized in the global minimum of the potential energy. In all simulations of mixed isotopic substitutions, we find that the heavier isotope is almost exclusively the participant in the hydrogen bond. © *2010 American Institute of Physics*. [doi:10.1063/1.3506027]

I. INTRODUCTION

Ammonia clusters are fundamental for a number of theoretically, practically, and economically important applications.[1–4] Therefore, ammonia clusters have been at the center of our investigative efforts for a number of years.[5–7] Our work has joined the experimental and theoretical endeavors of a growing community.[8–29] Experimental[8–15] and theoretical[16–22] investigations abound in the literature. The main focus of the experimental work has been on the dimer and on the condensed phase.[26–29] The experimental work has been accompanied by a systematic development of numerous potential energy models to study and reproduce spectroscopic properties of small clusters.[23–25]

The ammonia dimer has been at the center of two controversies in the literature regarding its rigidity and its structure. Assuming a rigid structure, the early experimental evidence[9, 10] has pointed to a surprising antiparallel structure in conflict with all theoretical predictions. The latter place the global minimum of the dimer in the classical linear hydrogen bond arrangement. Both these controversies have been addressed by a number of high level theoretical investigations of the vibration–rotation–tunneling states from a set of sequentially refined potential energy surfaces. The most refined of these[23] is capable of computing the far infrared spectrum including many lines not involved in the fitting procedure, the effects of off diagonal Coriolis interactions, and hindered umbrella inversion splittings. The outcome of these careful theoretical investigations yields a hydrogen bonded structure bent away from the classical linear configuration and with a highly nonrigid character. The highly nonrigid character, typical of many weakly bound dimers, explains the appar-

ent disagreement between the global minimum structure obtained from *ab initio* calculations and the vibrationally averaged structure deduced from the microwave spectroscopy experiments. Ammonia clusters have been grown in helium nanodroplets[14] at 0.38 K, and their infrared spectra confirm that as few as 1000 molecules are sufficient to produce a structure similar to the crystal structure of the bulk. More recent investigations have focused on the vibrational spectra of small- to mid-sized ammonia clusters,[20, 22] where particular intramolecular bands sensitive to clustering and the coordination number on the ammonia molecules have been identified.

Equilibrium geometries, interaction energies, and harmonic frequencies of the isomers in the ($n = 2$–5) range have been determined by one of our groups using correlated *ab initio* calculations at the second order Møller-Plesset perturbation theory level (MP2) with Dunning's aug-cc-pVXZ (X = D, T, Q) basis sets and the counterpoise procedure. The effect of zero point energy (ZPE) on the relative stability of the clusters using harmonic frequencies have been computed for a number of isomers. The magnitude of many-body effects have been determined to account for 10%–15% of the total interaction energy, whereas the 4-body effects can be neglected as a first approximation.[5] In the aforementioned study we also determine that freezing the monomer structure to its gas phase geometry only has a weak impact on the energetic and structural properties of the clusters.

Based on the data obtained from the study in Ref. 5, we have constructed an analytical model to describe the interaction between rigid ammonia molecules including the explicit description of induction. The description of polarization effects in the analytical model is introduced by using a noniterative form of the "charge on a spring" model. The resulting potential energy surface can be explicitly differentiated as a consequence of the noniterative form of the polarization effects. The minima of the ammonia clusters in the ($n = 3$–20)

a)Author to whom correspondence should be addressed. Electronic mail: curotto@arcadia.edu.
b)Also at University degli study dell' Insubria, Via Giuseppe Garibaldi, 61, 22100 Como, Italy. Electronic mail: mellam@cardiff.ac.uk.

range have been searched in the same work.[6] In a more recent study,[7] we perform classical and quantum finite temperature simulations of ammonia clusters in the ($n = 2$–11) range using the stereographic projection path integral (SPPI) method. The latter is an exact approach to perform quantum N, V, T ensemble simulations for clusters of rigid bodies.[30–41] When the SPPI method is implemented together with the random series approach[42–48] and the finite difference estimators of Predescu *et al.*,[45] the physical attributes converge to third order in the number of series coefficients.

From the SPPI simulations we learn that the quantum effects on the binding energy are substantial for ammonia clusters as previously found for water. By using the converged ensemble energy at 40 K, we estimate that the ZPE is approximately 35% of the binding energy for the largest sizes and climbs as we move toward smaller sizes to approximately 50% for the dimer. The quantum evaporation energy estimate [$\langle E_n(T = 40\,\text{K})\rangle - \langle E_{n-1}(T = 40\,\text{K})\rangle$] suggests the possibility of an enhanced kinetic stability for certain sizes compared to the others. The behavior of the structural and thermodynamic properties as a function of temperature for $(\text{NH}_3)_{2-11}$ has led us to conclude that several clusters in that size range, including the dimer, pentamer, and hexamer, are highly fluxional compared to other sizes and to other types of molecular clusters, in agreement with mounting experimental evidence.[9–13] The recent SPPI study of ammonia clusters has yielded a plethora of valuable information. However, from path integral simulations alone it is hard to know exactly how much of the energy is in excess of the global minimum from thermal excitation and how much is from the zero point energy at any finite temperature. It is well known that the Feynman path integral method becomes progressively less efficient as lower values of the temperature are considered and that simulations at temperatures dominated by a ground state are unfeasible.

The main objective for the work reported here is to obtain the energy and the structural character of the ground state for several small ammonia clusters. The present work fills in the gaps in our knowledge of the behavior of small ammonia clusters that the work in Ref. 7 leaves behind. An estimate of the lowest energy achievable by ammonia clusters of various sizes is more feasible when the goal is to obtain a precise and accurate measure of the relative stability for different sizes at temperatures below 10 K. A quantitative measure of relative stability in turn allows one to predict what species dominate when clusters are generated experimentally under the simulated conditions. Jet expansion temperatures can be as low as a few Kelvin, whereas growth in nanodroplets is typically at a fraction of a degree Kelvin. Finite temperature quantum simulations of ammonia clusters at these temperatures are formidable tasks.

In comparing the energy of the ground state with the energy at 40 K obtained by path integral simulations and studying how the thermal excitation energy in excess of the ZPE changes with size, we hope to obtain a qualitative measure of the relative density of excited states for several small ammonia clusters. In particular, we are interested to learn if the fluxional behavior of the dimer and the pentamer is correlated with the thermal excitation energy in excess of the ZPE and

what role is played by the acceptor donor–donor acceptor exchange. For the latter question we note that the structure of the global minima in the ($n = 3$–5) range all have equivalent molecules that result from the high symmetry of the structures and the low dimensionality of the aggregates. In the trimer, tetramer, and pentamer, all the molecules are acceptor–donors of hydrogen bonds. The dimer is unique with one acceptor and one donor molecule.

The uniqueness of some locations for ammonia molecules, coupled with the exploration of isotopomers to achieve a degree of uniqueness among the moieties, is a fertile ground for exploration of deep questions at the core of the nature of the hydrogen bond. Therefore, we find the exercise of characterizing the ground state wavefunction for the dimer through the pentamer with selected isotopic substitutions particularly insightful. Additional important questions that can be answered in a straightforward manner by our methods are as follows: (a) are the ground state wavefunctions localized in one single well or in multiple wells of the potential energy surface? (b) A cluster of ammonia is described by two sets of degrees of freedom: the molecular translations and the molecular orientations relative to the laboratory axis. How are these two sets affecting the shape and the spread of the wavefunction?

We find the aforementioned questions particularly timely given two recent advancements[35,39] for the implementation of variational Monte Carlo (VMC) and diffusion Monte Carlo (DMC) simulations in non-Euclidean manifolds contributed by our groups. The non-Euclidean manifolds result from our use of rigid bodylike constrains for the molecular tops in our simulations. Our DMC methods are based on the construction of the velocity distribution by rejection techniques and are capable of functioning in a broad class of non-Euclidean spaces generated by holonomic constraints. Our formulation avoids the use of Lagrange multipliers and it is derived from the Feynman quantization in manifolds[49–52] proposed by DeWitt.[53] In a second article[39] we propose and test several importance sampling strategies for stereographic projection DMC in manifolds. We use a family of one parameter optimized trial wavefunctions for VMC in stereographically projected manifolds to produce the importance sampling. We find the same advantages in using importance sampling functions for the diffusion Monte Carlo simulations in manifolds as one finds in Euclidean spaces mapped with Cartesian coordinates. Additionally, our proposed family of trial wavefunctions can help to overcome problems with nonconfining potentials and can suppress quasiergodicity effectively. The use of intramolecular constraints in a molecular cluster are essential to overcome the inevitable stiffness resulting from the difference in the fundamental frequencies between the intramolecular and intermolecular degrees of freedom. Therefore, without these recent developments, it would be particularly challenging to carry out DMC simulations for aggregates of molecular tops.

The rest of the article is organized as follows. In Sec. II, we briefly review the VMC and DMC strategies for non-Euclidean manifolds. These methods have been derived in detail elsewhere.[35,39] In Sec. II, we also describe several modifications that we find necessary for the structural

characterizations of the random walks.[54] Our results are in Sec. III and the conclusions are in Sec. IV.

II. METHODS

Each NH_3, NH_2D, or ND_3 monomer is treated as a rigid body and use of Cartesian coordinates is made for the location of the center of mass of the monomer, and three stereographic projections are used to specify the monomer orientation relative to the laboratory axis.[7,30–41] The mapping from Euler angles to quaternions and to stereographic projections has been worked out in detail elsewhere.[41] The number of dimensions of the space is $6n$ for n monomers, and the space is a differential manifold with an associated Hessian metric tensor $g_{\mu\nu}$. Unlike in Euclidean spaces mapped with Cartesian coordinates, the latter does not equal the diagonal matrix with masses as eigenvalues. Rather, it is a symmetric matrix that varies in value from point to point in the space regardless of the system of coordinates used to map the space.[55] We have found that there are less technical difficulties in using the stereographic projections for quantum Monte Carlo simulations of rigid bodies. The main reason is that, unlike the more traditional Euler angles or quaternions, the stereographic projection coordinates extend from $-\infty$ to $+\infty$. We use these coordinates for all three types of simulations performed in the present work.

The form of the trial wavefunction used for the VMC and DMC simulations is[39]

$$\Psi_T = \exp(-\beta V/2), \tag{1}$$

where β is the only parameter to be optimized and V is the system potential energy.[6] To optimize β, we average the local energy estimator

$$\Psi_T^{-1}\mathcal{H}\Psi_T = V - \frac{\hbar^2}{2}\left\{\frac{\beta^2}{4}g^{\mu\nu}\partial_\mu V \partial_\nu V - \frac{\beta}{2}g^{\mu\nu}\partial_\mu\partial_\nu V \right.$$
$$\left. - \frac{\beta}{2}\left\{g^{\mu\nu}[\partial_\mu \ln g^{1/2}] + \left(\frac{\partial}{\partial x^\mu}g^{\mu\nu}\right)\right\}\partial_\nu V\right\}, \tag{2}$$

$$\langle E\rangle_{\text{VMC}} = \frac{\int dq\, g^{1/2}(\Psi_T^{-1}\mathcal{H}\Psi_T)|\Psi_T|^2}{\int dq\, g^{1/2}|\Psi_T|^2} \tag{3}$$

for several values of the parameter β. In Eqs. (1) and (2), g is the determinant of $g_{\mu\nu}$.

All the VMC calculations consist of 21 independent runs; in each run, a total of 2×10^6 moves are performed using parallel tempering[56–59] with 40 walkers distributed evenly in temperature from $T = 10$ K up to 300 K. The value of T at which the average local energy has the lowest value, or alternatively, when its fluctuations are at a minimum, corresponds to the optimal parameter β of our trial wavefunction,

$$\beta = (k_B T)^{-1}, \tag{4}$$

where k_B is Boltzmann's constant. The quantity in Eq. (3) and the equation below,

$$\langle V\rangle_{\text{VMC}} = \frac{\int dq\, g^{1/2}V(q)|\Psi_T|^2}{\int dq\, g^{1/2}|\Psi_T|^2}, \tag{5}$$

evaluated at the optimal parameter represents, respectively, the best estimate of the total and potential energy in the ground state. A VMC move is either a swap with a walker at an adjacent temperature, or else we select at random one of the n monomers using a uniform distribution, and we move at random all six of its degrees of freedom at once.

The first million moves serve to equilibrate all the walkers and reach the asymptotic distribution. The second million moves are used to accumulate values of the local energy estimator in Eq. (2). The results obtained from each independent block are averaged, and the statistical error of the averages is obtained using twice the standard error in the mean.

The result of the VMC calculation is not only a best estimate (upper bound) of the true ground state energy, it also contains the optimal wavefunction for the importance sampling of the diffusion Monte Carlo simulation.[60–63] The importance sampling scheme we employ in this work is that suggested by Kalos et al.,[60] where we simply correct the branching function w after the diffusion move $q \rightarrow q'$,

$$w = \frac{\Psi_T(q')}{\Psi_T(q)}\exp\left\{\frac{1}{2}[V(q) + V(q')-2E_{\text{ref}}]\Delta\tau\right\}. \tag{6}$$

E_{ref} is the reference energy (essentially, an estimate of the ground state energy). E_{ref} is adjusted with a feedback equation to achieve a steady-state for the population of replicas after the entire population is subjected to diffusion and branching moves.[62] The exact ground state energy is obtained by averaging the estimator in Eq. (2) over the population of replicas.

The additional complication for our application of DMC comes from the differential manifold over which the diffusion takes place.[39] Since we use rigid ammonia monomers, the metric tensor $g_{\mu\nu}$ enters into the diffusion part of the algorithm as we seek to obtain a distribution of diffusion steps Δq from

$$p(\Delta q) = A \exp\left\{-\frac{g_{\mu\nu}(q)\Delta q^\mu \Delta q^\nu}{2\Delta\tau}\right\}. \tag{7}$$

In Eq. (7), A is a normalization constant, $\Delta\tau$ the (imaginary) time interval, and $g_{\mu\nu}(q)$ the metric tensor with its spacial dependence represented explicitly as its argument (q). The metric tensor is the effective mass of the system. The fact that $g_{\mu\nu}$ changes from point to point in the manifold over which diffusion takes place changes the shape of the distribution $p(\Delta q)$. The result is that the Δq is no longer a Gaussian random variable and the sampling of the function in Eq. (7) has to be performed with rejection techniques.[35,39] Since the correct shape of the distribution of $\{\Delta q^\mu\}_{\mu=1}^{6n}$ depends on the correct distribution of the variables $\{q^\mu\}_{\mu=1}^{6n}$, namely, $\Psi_T\Psi_0$, and these two sets of variable are independent, there are several possibilities for the acceptance–rejection probability. These have been systematically considered previously.[35]

The acceptance–rejection procedure for the production of deviates Δq^μ distributed according to Eq. (7) has been subjected to relatively rigorous tests on simple monodimensional systems[35,39] and has been implemented to study the Stockmayer trimer[39] and the water octamer.[40] In those applications we find no difficulty in generating the proper diffusion step distributions. In the present investigation, however, we find that the ammonia dimer and pentamer are particularly

challenging systems because of their highly fluxional nature. When the rigid molecular tops have as wide a probability density over rotation degrees of freedom as the dimer displays in Fig. 4, for example, the corresponding stereographic projections q^μ take values inside a very large interval $-L \leq q^\mu \leq L$ if the reference frame is fixed.[31] The Hessian metric is such that

$$\lim_{|q| \to \infty} g_{\mu\nu}(q) \to 0. \tag{8}$$

In those limits, the corresponding distribution in Eq. (7) becomes very wide and sampling it with rejection techniques becomes very inefficient. There is a simple remedy for the aforementioned problem, which consists of frequently changing the frame of reference that defines the stereographic projections.[31] To change the frame of reference we simply rotate each replica in the population, meaning the cluster as a whole, or equivalently the laboratory axes are reoriented prior to the diffusion step. These rotations are finite and by random amounts and must be implemented before the computation of the stereographic projections of the rigid molecules relative to this new frame can be carried out. This simple remedy relies on the rotational invariance of the potential and successfully produces the proper step distribution stabilizing the diffusion algorithm.

Results from the SPPI calculations are compared to the DMC estimate with the converged value of the thermal energy at a sufficiently low temperature. We use the $(NH_3)_2$ and the $(ND_3)_2$ system to push the convergence of the estimator for $\langle E \rangle$ to cold temperatures beyond those achieved in our earlier explorations,[7] in order to compare with the energy that DMC yields for the ground state. Our approach to model diffusion in curved manifolds is relatively recent, and in light of the additional difficulties mentioned earlier, we carefully test its performance using two dimers. The SPPI technique has been developed and tested on a number of systems[30–34,36–38] and is used in the present investigation in conjunction with the reweighted random series technique[42–48] and the finite difference estimator for the energy and the heat capacity.[45]

A. The structural comparison algorithm for $(NH_3)_n$

The comparison between two configurations of a cluster is carried out with the structural comparison algorithm[54] (SCA), which has been modified for the present work. If the configurations to be compared belong to a system that contains n indistinguishable ammonia molecules, then the approach we use is traditional.[54] We have recently modified the basic approach to handle molecular clusters.[40] Since some of the systems we simulate here contains distinguishable parts, we have to make further modifications. Therefore, it is convenient to reproduce the details of the approach as adapted to molecular clusters with indistinguishable components.[40]

Let $\{r_k^{(A)}\}_{k=1}^{4n}$ and $\{r_k^{(B)}\}_{k=1}^{4n}$, respectively, denote the $12n$ Cartesian coordinates for two configurations A and B of a $(NH_3)_n$ cluster. In essence, the goal of the algorithm is to find the location and orientation of B that minimizes the sum of all radial differences

$$\sum_{k=1}^{4n} \left| r_k^{(A)} - r_{k'}^{(B)} \right|. \tag{9}$$

In pseudocode the algorithm constitutes the following steps:

1. Configurations A and B are translated so that the origin is the center of mass.
2. Configurations A and B are rotated so that atom 1 and i, respectively, are on the z axis ($1 \leq i \leq 4n$) and so that atom 2 and j for configurations A and B, respectively, are on the $x - z$ plane ($1 \leq j \leq 4n$, $j \neq i$).
3. For each of the $4n(4n - 1)$ rotations, a sorting of the atoms is performed to find the atom of B that is the closest to atom k of A, for $k = 2, \ldots, 4n$. The SCA metric is the infimum of the set

$$\Delta_A = \inf\{\Delta_{ij}(A)\}_{i,j=1,i\neq j}^{4n}, \tag{10}$$

where $\Delta_{ij}(A)$ represents an element of the following set of sums:

$$\Delta_{ij}(A) = \sum_{k=1}^{4n} \left| r_k^{(A)} - \mathcal{P}\mathbf{R}(\Omega_i, \Omega_j) r_k^{(B)} \right| \tag{11}$$

and the element of the set $\{\mathcal{P}\mathbf{R}(\Omega_i, \Omega_j) r_k^{(B)}\}_{k=1}^{4n}$ is the configuration B rotated and with the labels permuted as described.

We refer to the metric in Eq. (10) as the all-atoms SCA distance. No distinction between N atoms and H atoms is made in its implementation. This geometric attribute is rotationally, translationally, and permutationally invariant among indistinguishable entities. In particular, the algorithm avoids searching through the $n!$ possible permutations of n identical particles and in its present form the computational efforts scales as n^4. The quantity Δ_A is most meaningful when the configuration A is a minimum or an important point of the potential energy surface. Δ_0 represents the all-atoms SCA distance from the system global minimum.

It has been our practice to compare distributions of the all-atoms SCA metric in Eq. (10) with the equivalent measure obtained by considering only the molecular centers.[40] In the present work, we find it useful to define a measure $\Delta_A^{(N)}$, as in Eq. (10) using only the Cartesian coordinates of the nitrogen atoms. We use the symbol $\Delta_0^{(N)}$ to represent the N-atom SCA distance from the system global minimum.

B. The structural comparison algorithm for $(ND_3)-(NH_3)_{n-1}$

We make one additional modification to study the geometric attributes of random walks produced while investigating $(ND_3)-(NH_3)_{n-1}$ systems. The comparison between two configurations A and B of a $(ND_3)-(NH_3)_{n-1}$ cluster is performed with the following steps.

Once more, we operate on the $12n$ Cartesian coordinates for two configurations A and B of a $(ND_3)-(NH_3)_{n-1}$ cluster $\{r_k^{(A)}\}_{k=1}^{4n}$ and $\{r_k^{(B)}\}_{k=1}^{4n}$, respectively.
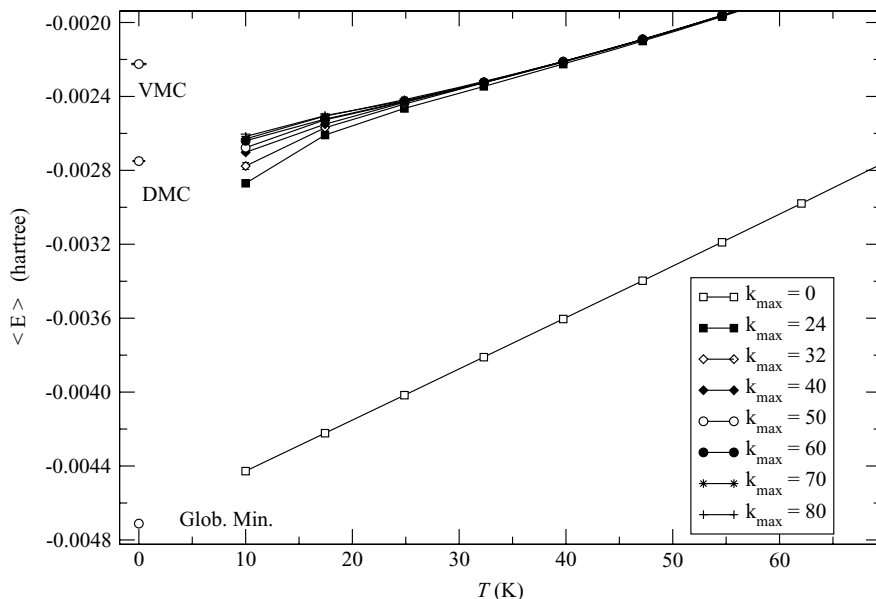
FIG. 1. Summary of the energy calculations for the NH$_3$ dimer. The white squares, labeled $k_{max} = 0$, are classical finite temperatures simulations results. All the other functions of temperature are results obtained with the SPPI for increasing values of k_{max} from 24 to 80. The white circles at $T = 0$ represent from bottom to top, respectively, the global minimum V_G, the ground state energy obtained by diffusion, and the estimate of the ground state energy obtained from the optimized Ψ_T [cf. Eq. (1)].

1. Configurations A and B are translated so that the nitrogen atom in the ND$_3$ moiety is at the origin.
2. Configurations A and B are rotated so that the C_3 vector is along the z axis. The C_3 vector points from the nitrogen atom of the ND$_3$ moiety toward the center of mass of the three deuterium atoms.
3. The resulting $12(n-1)$ Cartesian coordinates of the (NH$_3$)$_{n-1}$ moiety are used to define the new SCA metric. Configuration A is rotated so that atom 1 in the (NH$_3$)$_{n-1}$ moiety is on the $x-z$ plane. Configuration B is rotated so that atom i in the (NH$_3$)$_{n-1}$ moiety is on the $x-z$ plane $1 \leq i \leq 4(n-1)$.
4. For each of the rotations in step 3, a sorting of the $4(n-1)$ atoms is performed to find the atom of B that is the closest to atom k of A, $1 < k < 4(n-1)$. The new SCA metric is the infimum of the set

$$\Delta_A^{(D)} = \inf \left\{ \Delta_i^{(D)}(A) \right\}_{i=1}^{4(n-1)}, \qquad (12)$$

where $\Delta_i^{(D)}(A)$ represent an element of the following set of sums

$$\Delta_i^{(D)}(A) = \sum_{k=1}^{4(n-1)} \left| \mathbf{r}_k^{(A)} - \mathcal{P}\mathbf{R}(\Omega_i)\mathbf{r}_k^{(B)} \right| \qquad (13)$$

and the element of the set $\{\mathcal{P}\mathbf{R}(\Omega_i)\mathbf{r}_k^{(B)}\}_{k=1}^{4(n-1)}$ contains the Cartesian coordinates of the (NH$_3$)$_{n-1}$ moiety for configuration B rotated and with the labels permuted as described in steps 3 and 4.

We use the symbol $\Delta_0^{(D)}$ to represent the all-atoms SCA distance from the system global minimum for the (ND$_3$)–(NH$_3$)$_{n-1}$ cluster obtained in this manner.

III. RESULTS

A. NH$_3$ dimer

Figure 1 contains all the values of the total energy of the NH$_3$ dimer from VMC, DMC, SPPI, and classical simulations at finite temperature. The white squares represent the classical N, V, T ensemble estimate of the thermal energy, and these extrapolate linearly to the global minimum. A range of values of k_{max} is shown in Fig. 1 from 24 to 80. Only the lowest temperatures are shown in Fig. 1 to emphasize the comparison between the finite temperature ensemble average and the ground state energy computed with DMC. The classical and quantum finite temperature simulations for values of k_{max} up to 40 are from our previous path integral simulations of the NH$_3$ dimer.[7] In the present work, we repeat the $k_{max} = 40$ simulation for consistency. With a $k_{max} = 40$ simulation, the heat capacity and the total energy converge at and above 40 K. In the present work we compare converged values of the energy at colder temperatures and consequently we find the need to systematically increase the values of k_{max} up to 80. At 10 K, the average energy obtained with $k_{max} = 80$ is statistically indistinguishable from that obtained with $k_{max} = 70$ and 60. Table I contains the energy values obtained by VMC (in column 2), DMC (in column 3), normal mode analysis about the global minimum (in column 4), path integral at 10 K, (column 5), and the global minimum energy (in column 6) for all eight of the species we simulate in the present work. The first row of table I contains the relevant energies for the NH$_3$ dimer. The VMC estimate of the ground state energy is 19% higher than the DMC value. The ZPE is 1.962 mhartree, and this amounts to approximately 42% of the binding energy. Unlike the classical calculation, which in Fig. 1 visibly extrapolates toward 0 K to the energy of the global minimum, the

TABLE I. Variational, diffusion, path integral, harmonic approximation for the ground state energy, and global minimum energies in hartree, for ammonia clusters in the dimer through pentamer range together with several selected deuterated species. The figures in parentheses are uncertain.

Species	VMC	DMC	Harmonic app.	SPI	Global minimum[a]
$(NH_3)_2$	−0.002 22(47)	−0.002 749(54)	−0.002 502	−0.002 61(66)[b], −0.002 21(18)[d]	−0.004 7718
$(ND_3)_2$	−0.002 944(3)	−0.003 182(70)	−0.003 057	−0.0031(40)[c]	—
NH_3–ND_3	−0.002 22(47)	−0.002 978(82)	−0.002 853	—	—
$(NH_3)_3$	−0.0080(58)	−0.009 20(89)	−0.008 829	−0.008 83(60)[d]	−0.0150 105
$(NH_2D)_3$	—	−0.009 93(52)	−0.009 320	—	—
$(NH_3)_2$–ND_3	−0.008 61(08)	−0.009 97(23)	−0.009 341	—	—
$(NH_3)_4$	−0.0144(08)	−0.016 08(10)	−0.015 54	−0.0155(75)[d]	−0.024 6860
$(NH_3)_5$	−0.0180(65)	−0.020 70(86)	−0.020 48	−0.0205(26)[d]	−0.032 2021

[a]From Ref. 6.
[b]Computed at 10 K.
[c]Computed at 4 K.
[d]At 40 K, from Ref. 7.

quantum simulations extrapolate to values at 0 K slightly below the DMC value graphed, indicating that the finite temperature energy reaches a plateau at lower temperatures, as expected. The normal mode frequencies λ_i are computed by diagonalizing the metric-weighted hessian $g^{-1/2} \left(\partial_\mu \partial_\nu V \right) g^{-1/2}$, where $g^{-1/2}$ is obtained by the Choleski decomposition. The ground state energy for each mode is added to the energy of the global minimum for each entry in column 4.

Our DMC simulations are all carried out with a target population size of 100 000 replicas. The first 1000 moves are used to reach the asymptotic distribution $\Psi_T \Psi_0$, where Ψ_T is in Eq. (1), and Ψ_0 is the true ground state of the system. The rest of the moves are used to sample the physical properties of interest. We first study the convergence of the algorithm with the time step $\Delta\tau$ used to produce the diffusion distribution in Eq. (7). For each value of $\Delta\tau$ we compute the average of 4 consecutive blocks of 250 population estimates after the first 1000 equilibration moves. We compute the error bars as twice the standard error in the mean from the block averages.

The values of $\langle E \rangle$ for the dimer obtained with a range of values of $\Delta\tau$ is graphed in Fig. 2. For $\Delta\tau \leq 120$ hartree^{-1}, the estimate of $\langle E \rangle$ is converged within the statistical error. The estimate of the ground state energy we report in Table I is obtained using a target population size of 100 000 replicas, $\Delta\tau = 20$ hartree^{-1}, with the equilibration period as explained earlier. The simulations are repeated 21 independent times and the block averages are used to compute the mean and its statistical error at the 95% confidence interval.

Additional insight can be gained by producing and comparing distributions of geometric properties extracted *a posteriori* from VMC and DMC simulations. These correspond to distributions of geometric estimators from $|\Psi_T|^2$ for VMC and $|\Psi_T \Psi_0|$ for DMC simulations. Three examples of these for the NH_3 dimer can be seen in Figs. 3–5. These graphs contain normalized histograms obtained after processing approximately 2.0×10^6 configurations from VMC (white circles) and DMC (black squares). The largest differences between the $|\Psi_T|^2$ and $|\Psi_T \Psi_0|$ distributions can be appreciated in the $|\Psi_T \Psi_0| (r_{NN})$ relative frequency in Fig. 3, where
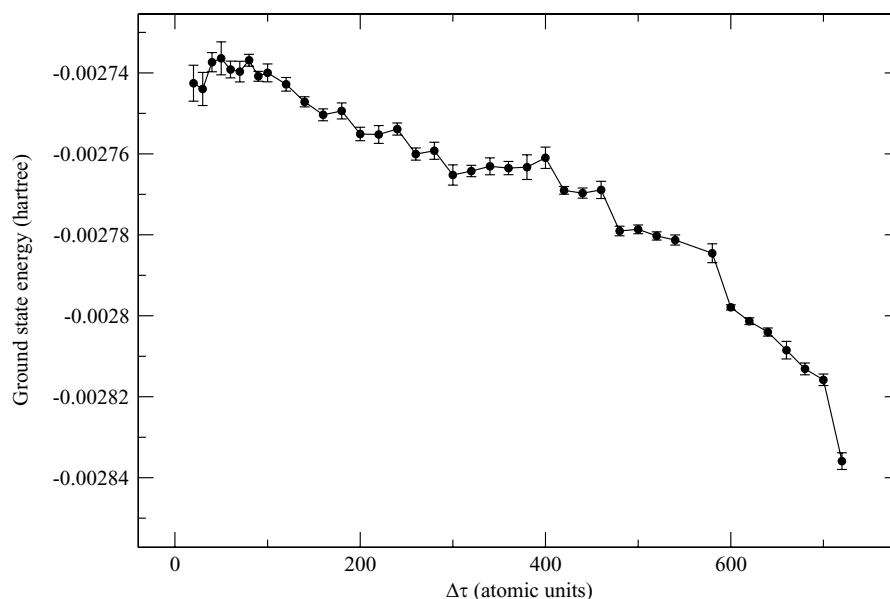

FIG. 2. Convergence profile of the DMC energy for the NH_3 dimer. The vertical axis is the estimate of the ground state energy in hartree, the horizontal axis is the diffusion time step $\Delta\tau$ in hartree^{-1}.
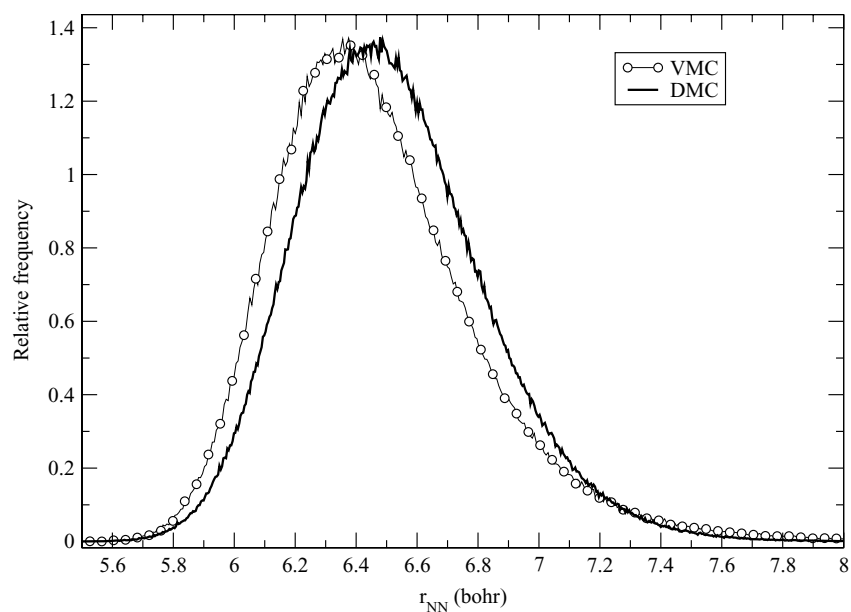
FIG. 3. Histograms of the N to N distance from VMC and DMC simulations of the ammonia dimer.

r_{NN} is the distance between the two nitrogen atoms. The two features have statistically identical full width at half height equal to 0.67 ± 0.01 bohr. The $|\Psi_T \Psi_0|(r_{NN})$ distribution peaks at 6.45 bohr, approximately 0.10 bohr higher than the $|\Psi_T|^2(r_{NN})$ peak. Figure 4 contains the graphs of $|\Psi_T \Psi_0|(\theta)$ and $|\Psi_T|^2(\theta)$, where θ is the angle between the two C_3 axis of the ammonia molecules, oriented from the N atom toward the center of mass of the three hydrogen atoms (cf. Fig. 7). The double feature that peaks at approximately $-90°$ and $+90°$ is indicative of the indistinguishable nature of the identical ammonia molecules which visit a donor–acceptor configuration with the same likelihood as the acceptor–donor configuration relative to the first molecule in our label list. The differences between the $|\Psi_T|^2(\theta)$ and the $|\Psi_T \Psi_0|(\theta)$ are min-

imal. The optimal trial wavefunction over-samples the linear configuration with the ammonia molecules pointing away from each other, compared to the actual ground state. Finally, Fig. 5 contains the distribution of Δ_0, the distance measured with the all-atoms SCA [cf. Eq. (10)], from the global minimum. Δ_0 includes differences among hydrogen atoms; consequently, it has far broader histograms in VMC and DMC simulations compared to those for r_{NN}. The $|\Psi_T|^2(\Delta_0)$ and $|\Psi_T \Psi_0|(\Delta_0)$ distributions are in good agreement. Additionally, both distributions of Δ_0 show some structure in the shape of a shoulder at approximately 7 bohr. To gain additional insight we inspect visually several configurations with graphical software and we compare these to the global minimum configuration. In the latter, the Newman projection along the
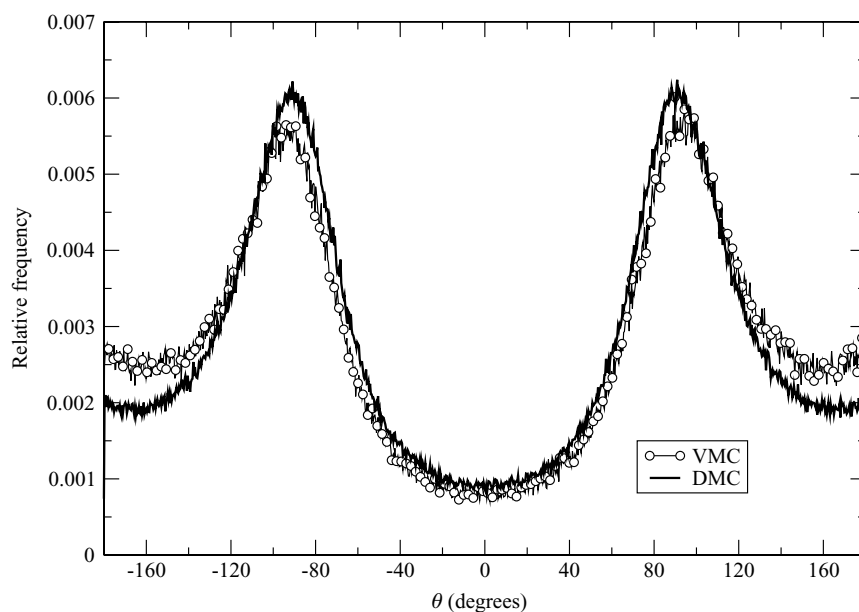

FIG. 4. Histograms of the angle θ between the two C_3 axis from VMC and DMC simulations of the ammonia dimer.
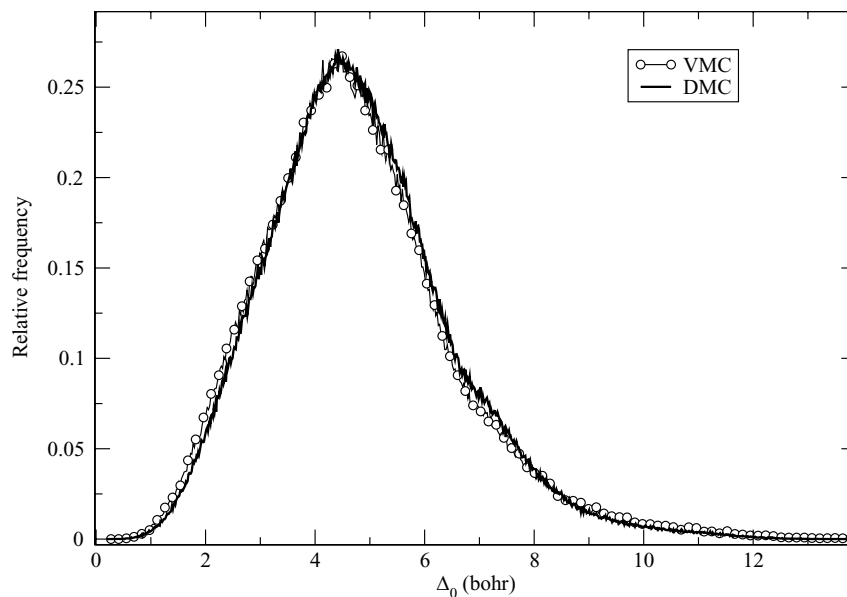
FIG. 5. Histograms of the SCA distance Δ_0 [cf. Eq. (10)] from VMC and DMC simulations of the ammonia dimer.

N–N vector, viewed from the donor to the acceptor, contains two hydrogen atoms on the acceptor, which eclipsed the two remaining hydrogen atoms on the donor molecule. A Newman projection is sketched in Fig. 7, where the dihedral angle Φ is defined. Because the three hydrogen atoms on the acceptor side are indistinguishable, we choose the smallest of all the possible dihedral angles when we measure Φ for a configuration. We find several minima of the dimer that have distinct values of Φ. The global minimum has a value of $\Phi = -12^o$.

The configuration with $\Phi \approx 0$ is dominant in the $|\Psi_T|^2 (\Delta_0)$ and $|\Psi_T \Psi_0| (\Delta_0)$ distributions. Furthermore, we determine that the shoulders around 7 in Fig. 5 in both of these is from a relatively smaller but significant number of acceptor–donor configurations for which $\Phi \approx -60^o$.
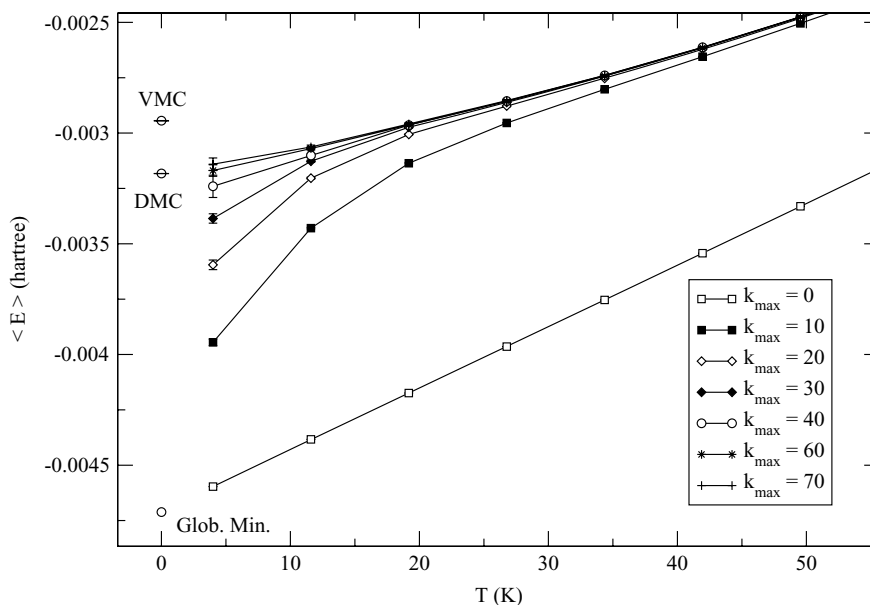
B. ND$_3$ dimer

We repeat all three simulations on the ND$_3$ dimer for one main reason. The agreement between the total energy at 10 K and at 0 K in the NH$_3$ dimer is not quantitative. In Fig. 1 we can see that the trend toward 0 K is qualitatively correct and that the extrapolation of these could yield reasonable agreement. However, we seek confirmation that our DMC results are quantitatively reliable and hold when compared with reasonable estimates of the ground state energy obtained in a different manner. Given that at 10 K the NH$_3$ dimer contains a small but significant amount of thermal energy, we are faced with the need of simulating at colder temperatures. We elect to simulate the ND$_3$ dimer and we extend the SPPI simulations to 4 K. The reasoning behind our choice is that the ND$_3$ dimer is more easily excited by thermal energy compared to the NH$_3$ dimer, making it a better system to simulate with path integral. At the same time, the energy level differences should be considerably smaller than the differences in the NH$_3$ dimer, pushing, hopefully, the amount of energy in excess of the ground state at 4 K below detection.

The graphs in Fig. 6 are the values of the total energy of the ND$_3$ dimer from VMC, DMC, SPPI, and classical simulations at finite temperature. The converged average total energy at 4 K is nearly statistically identical to the DMC estimates. The energy at 4 K, for $k_{max} = 70$, the DMC estimate, VMC, and harmonic analysis estimates of the ground state energy are found in the second row of Table I. The best VMC energy is 7.5% higher than the best estimate of the ground state energy. Additionally, the ratio of the two ZPEs (1.529 mhartree for the ND$_3$ dimer) is 0.7793. The ratio of the two ZPEs is close to $2^{-1/2}$, the result expected for a harmonic system if the hydrogen degrees of freedom dominate the quantum effects.

We inspect graphs of $|\Psi_T|^2$ and $|\Psi_T \Psi_0|$ (not shown) along the same three degrees of freedom, r_{NN}, θ, and Δ_0 and we obtain the same qualitative information from them. The VMC and DMC histograms for r_{NN} agree better for the ND$_3$ dimer than they do for the NH$_3$, dimer, whereas the converse is true for the VMC and DMC histograms of Δ_0. These graphs for the ND$_3$ dimer contain a similar shoulder created by a comparable amount of twisted configurations $\Phi \approx -60^o$, as it is seen in the VMC and DMC histograms for the NH$_3$ dimer. The DMC distribution peaks at smaller values and has a relatively less intense shoulder at 7 bohr compared to the NH$_3$ dimer.

C. ND$_3$–NH$_3$ dimer

The VMC estimate of the ground state energy of the ND$_3$–NH$_3$ dimer (found in the third row of Table I) is 25% greater than the DMC estimate. This is the largest discrepancy between VMC and DMC among the three dimers. We do not carry out SPPI simulations for the ND$_3$–NH$_3$ dimer. Rather, we concentrate on characterizing the VMC and the DMC walks and compare several histograms of geometric properties generated from them. The histograms of r_{NN} and θ look similar to those for the other two dimers. The structural

FIG. 6. VMC, DMC, and SPPI estimates of $\langle E \rangle$ for the ND$_3$ dimer.

effects of the isotopic substitution are better evidenced by the following two vector projections. Let $\mathbf{C}_{H,i}$ be the center of mass of the three hydrogen atoms in molecule i, and let $\mathbf{R}_i$ be the position of the nitrogen atom in molecule i. Then the vector

$$\mathbf{C}_{3,i} = \mathbf{C}_{H,i} - \mathbf{R}_i \tag{14}$$

is along the C_3 axis, and its size is constant and equal 0.727298 bohr since the ammonia molecule is treated as a rigid body. The index i in Eq. (14) is simply a label for the molecule number in the cluster. For the NH$_3$–ND$_3$ dimer, it is possible to label uniquely the NH$_3$ moiety as the $i = 1$ molecule and the ND$_3$ moiety as the $i = 2$ molecule. Using these labels and the definition for the respective $\mathbf{C}_{3,i}$, we construct two scalar projections,

$$p_{12} = \frac{(\mathbf{R}_2 - \mathbf{R}_1) \cdot \mathbf{C}_{3,1}}{|\mathbf{R}_2 - \mathbf{R}_1|}, \tag{15}$$

$$p_{21} = \frac{(\mathbf{R}_2 - \mathbf{R}_1) \cdot \mathbf{C}_{3,2}}{|\mathbf{R}_2 - \mathbf{R}_1|}. \tag{16}$$

The possible range of values for the projections p_{12} and p_{21} are from $-|\mathbf{C}_{3,i}|$ to $|\mathbf{C}_{3,i}|$ or $-0.727298 \leq p_{12}, p_{21} \leq 0.727298$ bohr. The vectors involved in the computations of these two properties are drawn in Fig. 7. If molecule 1 and 2 are indistinguishable, then the histogram of the two projections should be identical. However, when quantum effects are considered, the ND–NH and NH–ND configurations are not degenerate and one expects to see differences between p_{12} and p_{21}. Since our trial wavefunction Ψ_T in Eq. (1) does not contain any information that can distinguish the NH$_3$ molecule from the ND$_3$ molecule, i.e., V is unchanged upon isotopic substitutions, we anticipate differences when we compare histograms of p_{12} and p_{21} from VMC and DMC simulations. The histograms produced from VMC and DMC walks for the two projections are in Figs. 8 and 9,

respectively. In Figs. 8 and 9 we note that the distributions from VMC walks are identical and have a double feature, a peak at -0.727298 bohr and a symmetric peak at 0.25 bohr. The DMC simulations are very different. The p_{12} distribution from DMC has a skewed peak at -0.727298 bohr and positive values have vanishing relative probabilities. This result indicates that the vector $\mathbf{C}_{3,1}$ (on the ND$_3$ moiety) is almost always aligned in the opposite direction from the $\mathbf{R}_2 - \mathbf{R}_1$ vector. Conversely, the p_{21} distribution has an intense peak at 2.5 and it vanishes as p_{21} approaches -0.727298 bohr. This result indicates that the vector $\mathbf{C}_{3,2}$ is almost always aligned in the same direction direction as the $\mathbf{R}_2 - \mathbf{R}_1$ vector. The two graphs in Figs. 8 and 9 strongly suggest that the ground state
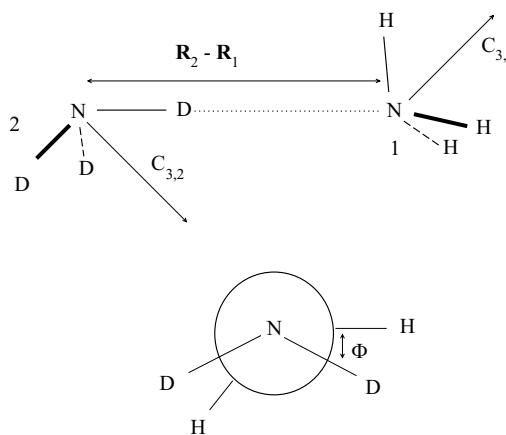

FIG. 7. A sketch of the vectors involved in the definition of p_{12} and p_{21} [Eqs. (15) and (16), respectively] for the ND$_3$–NH$_3$ dimer. The covalent bonds represented by heavy lines are pointing out of the page toward the reader, those represented by dashed lines point away from the plane of the page, and the dotted line represents the hydrogen bond. In the global minimum, the D–N–N–H torsional angle obtained with the two heavy lines (or the two dashed lines) is close to zero.
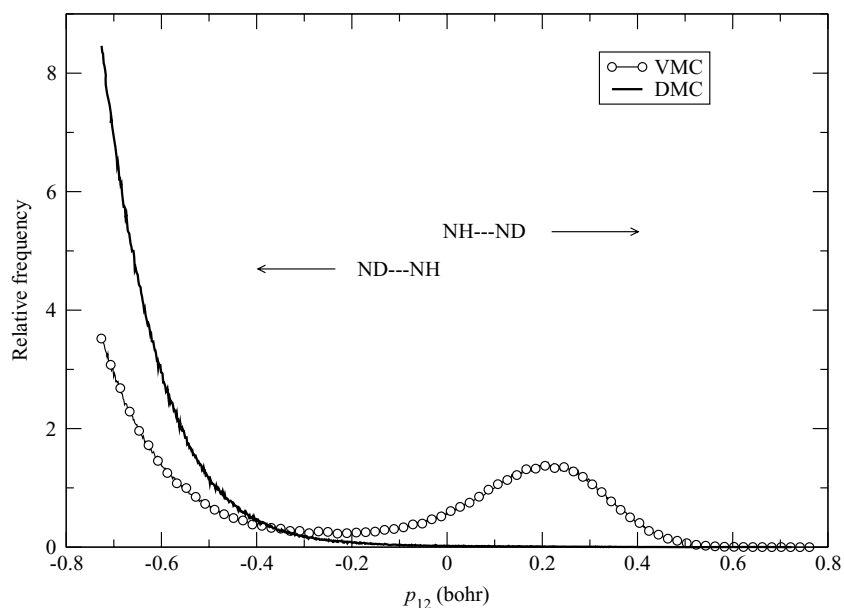
FIG. 8. Histograms of the p_{12} projection [cf. Eq. (15)] from VMC and DMC for the ND_3–NH_3 dimer.

of the ND_3–NH_3 is preferentially in the ND–NH donor to acceptor configuration.

We gather additional supporting evidence that the ND_3 moiety is preferentially in the donor position by inspecting graphs of the SCA metric $\Delta_0^{(D)}$ defined in Eq. (12). Figure 10 contains graphs of the distributions of $\Delta_0^{(D)}$ obtained from 2 $\times 10^6$ configurations generated by VMC walks (white circles). The latter distribution is compared with histograms of $\Delta_0^{(D)}$ obtained from approximately 2×10^6 replicas from DMC. Visual inspection of several configurations with $\Delta_0^{(D)} \approx 36$ bohr confirms that these are NH_3 donor–ND_3 acceptor configurations. This peak is conspicuous in the VMC distribution but absent in the DMC one. The two features at $\Delta_0^{(D)} \approx 4.2$ bohr and $\Delta_0^{(D)} \approx 7.5$ bohr are all ND_3 donor–NH_3

acceptor configurations with two different values of Φ similar to the other two dimers.

D. NH_3 trimer through the pentamer

In Table I, the values of the VMC and DMC energy can be conveniently compared with the respective values of the global minima reproduced from Ref. 6, and the values of the energy at 40 K reproduced from Ref. 7. Inspection of the distributions of $\Delta_0^{(N)}$ from $|\Psi_T|^2$ (white circles) and $|\Psi_T \Psi_0|$ (dark lines) in Fig. 11, as well as visual inspections of numerous configurations, confirms that both the ground state and the variational wavefunctions are confined to planar ringlike configurations similar to the respective global
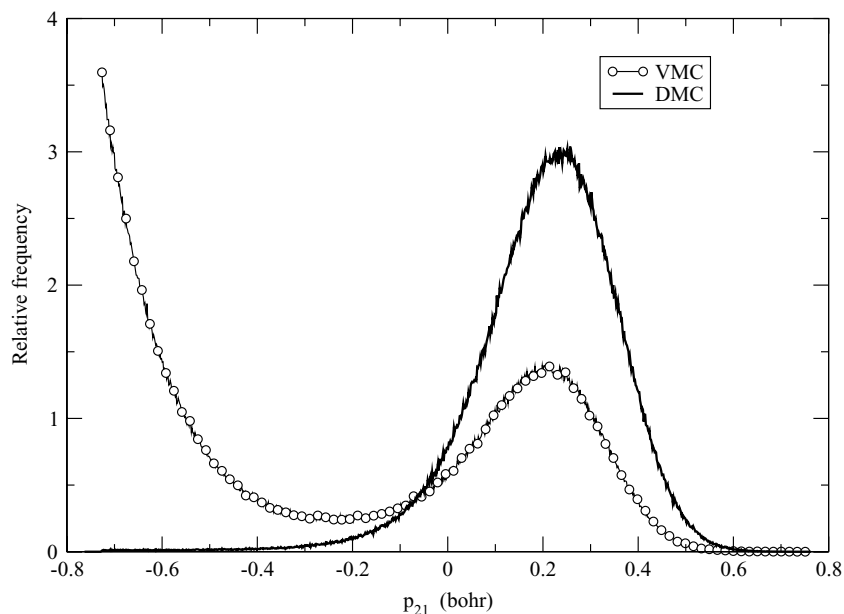

FIG. 9. Histograms of the p_{21} projection [cf. Eq. (16)] from VMC and DMC for the ND_3–NH_3 dimer.
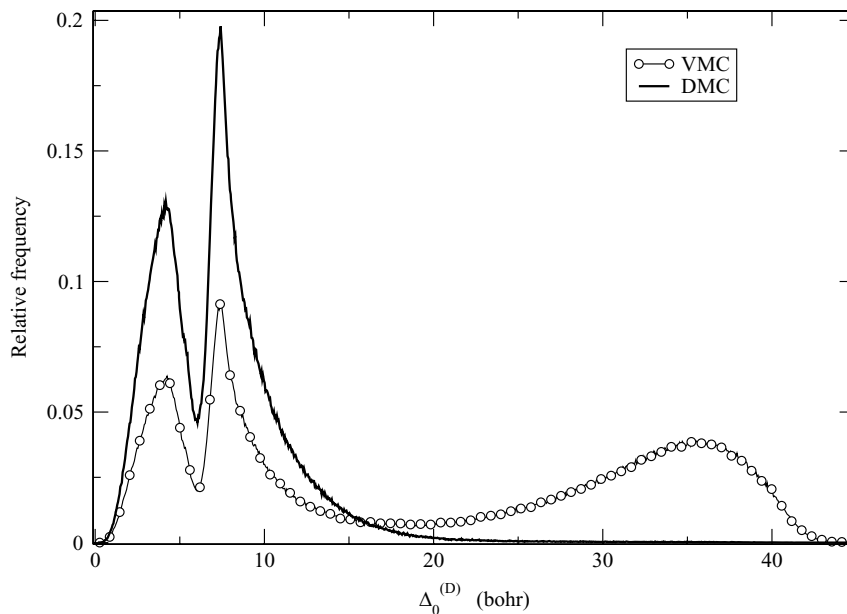
FIG. 10. Histograms of the SCA distance $\Delta_0^{(D)}$ (cf. Sec. II B) from VMC and DMC simulations of the ND$_3$–NH$_3$ dimer.

minima for the trimer and the tetramer.[6] The $\Delta_0^{(N)}$ distribution from VMC simulations of the pentamer shows a significant feature at 10.5 bohr which is absent in DMC simulations. The VMC wavefunction of the pentamer contains a significant amount of nonplanar configurations. These contribute to the peak at 10.5 bohr in the VMC distribution. Given that the $\Delta_0^{(N)}$ values measured from $|\Psi_T \Psi_0|$ distributions do not display a double feature and that the single peak at 3 bohr is a planar configuration, we conclude that the pentamer ground state wavefunction is predominantly planar as well.

Results from VMC and DMC simulations for the Δ_0 distributions are in Fig. 12. The Δ_0 distribution from VMC and

DMC for the trimer are in relatively good agreement, and the distributions from VMC appear sharper than those from DMC compared to the remaining two systems. This is true for both $\Delta_0^{(N)}$ in Fig. 11 and for the Δ_0 distribution in Figs. 12 and 3. The behavior of the VMC wavefunction as a function of cluster size correlates with the trend of the optimal parameter β for ψ_T. The graphs in Fig. 13 display the behavior of the variational energy estimate as a function of $T = (k_B \beta)^{-1}$ for (NH$_3$)$_{2-5}$. The values of T that yield the best $\langle E \rangle_{\text{VMC}}$ systematically increase from 100 to 130 K, 150 and 160 K for the dimer to the pentamer, respectively.

In Fig. 12 the DMC distributions for the trimer and tetramer have a main peak, the location of which grows as
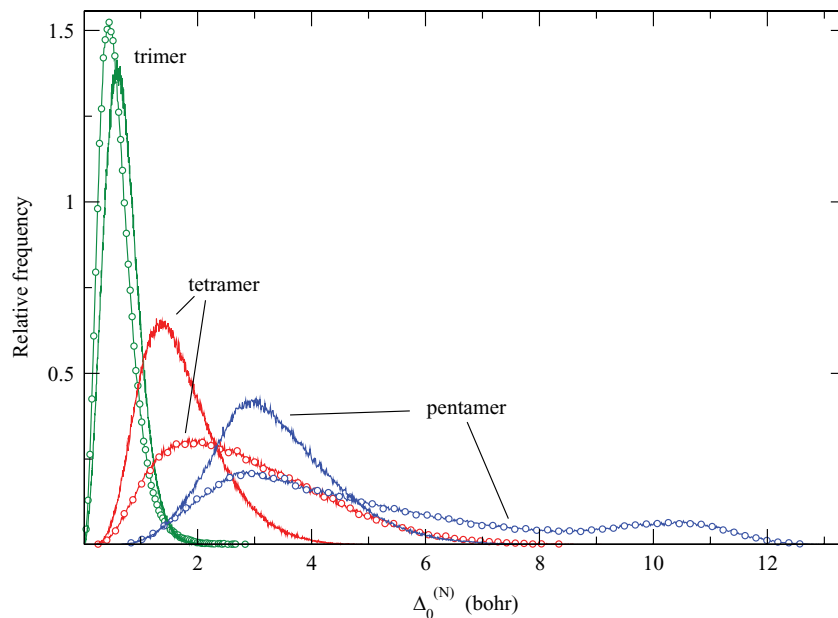

FIG. 11. Histograms of the SCA distance $\Delta_0^{(N)}$ (cf. Sec. II A) from VMC (open circles) and DMC (solid lines) simulations of the (NH$_3$)$_{3-5}$.
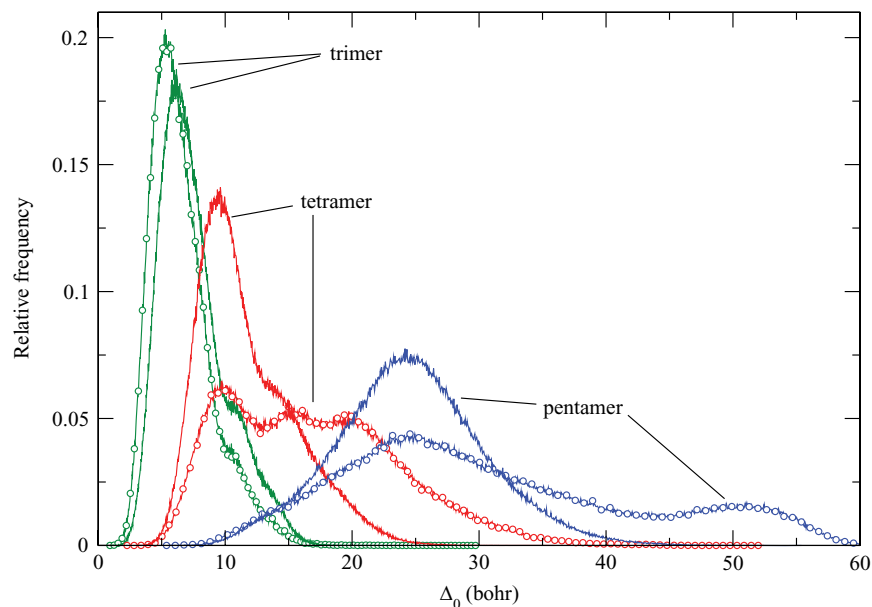
FIG. 12. Histograms of the SCA distance Δ_0 [cf. Eq. (11)] from VMC (open circles) and DMC (solid lines) simulations of $(NH_3)_{3-5}$.

a result of the increase of the number of atoms [cf. Eq. (11)]. Both curves have a shoulder toward higher values of Δ_0, attributable to a significant amount of twisting of the axial hydrogen atoms. These features are similar to those we observe in the dimers. The Δ_0 distribution for the DMC simulation of the pentamer, however, shows a large shift in the peak, and in its width, indicating that the hydrogen atoms have a much higher degree of fluidity for the pentamer compared to the smaller clusters.

E. Isotopically substituted trimers

Lastly, we perform VMC and DMC simulations on two distinct trimer with three of the nine hydrogen atoms replaced by deuterium atoms. The two species we study are $(NH_3)_2-ND_3$, where all three deuterium atoms are on one moiety, and the cluster $(NH_2D)_3$, where all three molecular tops are identical and each moiety contains one deuterium atom. We choose $(NH_2D)_3$ for DMC simulations after learning that the NH_3 trimer is a relatively rigid equilateral ring, with all three equivalent positions having a donor–acceptor role. The specific question we address with the results from the $(NH_2D)_3$ structures obtained in the DMC simulation is clear. Is the deuterium preferentially taking part in the hydrogen bonding? If the ground state wavefunction of the $(NH_3)_2-ND_3$ cluster is still a ringlike structure, then clearly, we cannot addressed the deuterium versus hydrogen preference in the donor position. Therefore, we expect one D–N
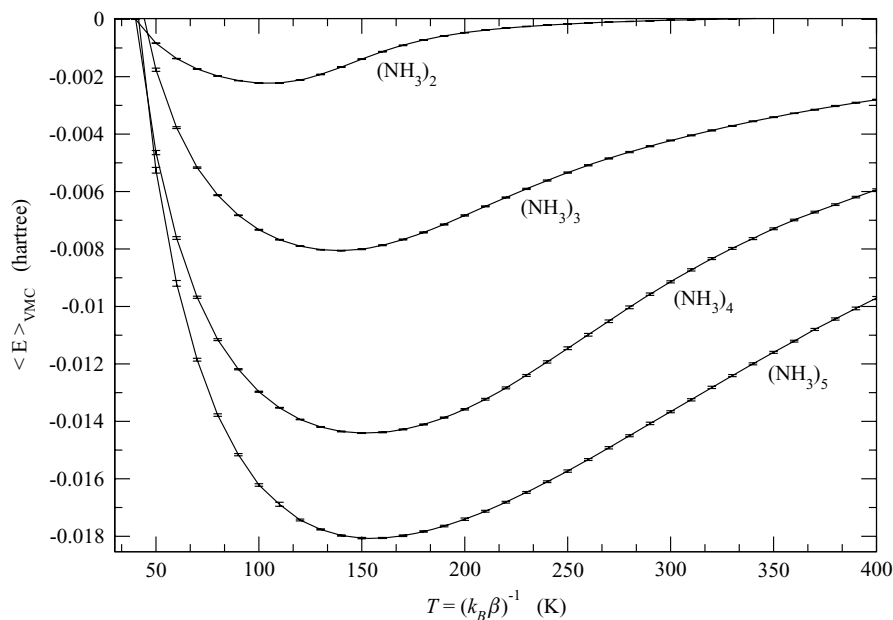

FIG. 13. Variational Monte Carlo energy at several values of the parameter $T = (k_B\beta)^{-1}$ [cf. Eq. (3)] for $(NH_3)_{2-5}$.
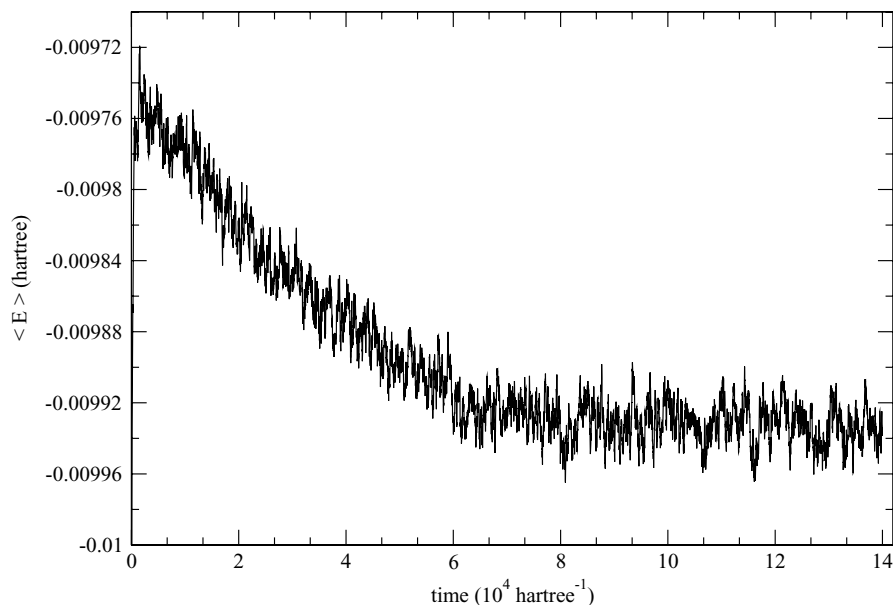
FIG. 14. Evolution of the DMC estimate of the ground state energy for the $(NH_2D)_3$ trimer. The data are obtained by starting from the optimal ψ_T obtained from VMC simulations of the $(NH_3)_3$ trimer, with a target population of 10^5 replicas, and with $\Delta\tau = 20$ hartree^{-1}. The data graphed are from one of the 20 repeated computations and includes 7000 consecutive diffusion-branching steps.

hydrogen bond in the ground state if its structure is the equilateral ring. However, we feel it is important to verify that the ground state wavefunction for $(NH_3)_2–ND_3$ is as expected from simple energetic and geometric arguments. We find it instructive to compare the ground state energy of the two systems, since both these energies should be lower than the value for the NH_3 trimer and the lowering effect should be primarily a mass effect. As a fact, the ground state energies of the two deuterated trimers, found in Table I, are relatively close to one another. Nevertheless, we are able to resolve a significant difference between them, thanks to the level of precision we achieve in our DMC simulations. Furthermore, simulating $(NH_3)_2–ND_3$, at least for the trimer, serves to understand the energetics of the NH_3-ND_3 exchange in the trimer. This substitution clearly has an impact on the equilibrium constant for its formation and on the preferential dissociation of a single molecule from the cluster.

There is no feature of the trial wavefunction in Eq. (1) that could distinguish among the three simulated trimers. Therefore, we expect the VMC energy of the $(NH_2D)_3$ and the $(NH_3)_2–ND_3$ clusters to be identical, and for the same reason, we expect the $|\psi_T|^2$ distributions to be very close to that of the NH_3 trimer. Consequently, we redo the variational calculation for the $(NH_3)_2–ND_3$ cluster simply to verify that the optimal energy is below that of the NH_3 trimer as a check, but we do not repeat the simulations for the $(NH_2D)_3$ cluster. Rather, for the latter we begin the DMC simulations from 10^5 configurations obtained from a variational calculation on the NH_3 trimer. We find that the guided DMC simulation for the $(NH_2D)_3$ cluster is relatively inefficient compared to the simulation of the regular trimer, or the $(NH_3)_2–ND_3$ system. To emphasize how the inefficiency is greater, we reproduce one of the 20 distinct simulations we perform on the $(NH_2D)_3$ cluster in Fig. 14. Unlike all the

other simulations, we note a slow and steady decrease of the population energy for the first 3000–4000 moves. The energy versus diffusion time graphed in Fig. 14 contains 7000 moves. To be certain that equilibration does take place we only choose to average the last 2000 moves when estimating the ground state energy. The results are highly reproducible over the 20 distinct repetitions, as the statistical error in Table I clearly indicates.

At the end of the 7000 moves we collect all the configurations for further analysis from all 20 repetitions. We end up with a total of 1 963 505 distinct replicas, which is close to the target 10^5 configurations multiplied by 20. To characterize the configurations we choose to collect and histogram together the following three deuterium to nitrogen distances (cf. the sketch in Fig. 15), $\mathbf{r}_{D_1-N_2}$, $\mathbf{r}_{D_1-N_3}$, and $\mathbf{r}_{D_2-N_3}$. We call the collective of these three distances simply $\mathbf{r}_{DN}$. The other two possibilities, namely, $\mathbf{r}_{D_3-N_2}$ and $\mathbf{r}_{D_3-N_1}$ are identical to $\mathbf{r}_{D_1-N_2}$, $\mathbf{r}_{D_1-N_3}$ since the three molecules are indistinguishable. If the deuterium atom is preferentially involved in the hydrogen bonding, as the sketch in Fig. 15 suggests, then there should be only two main values of the distance, that from the deuterium atom to the nitrogen atom in the intermolecular bond (such as $\mathbf{r}_{D_1-N_2}$, and $\mathbf{r}_{D_2-N_3}$) and that between a deuterium atom in the plane and a nonneighboring nitrogen such as $\mathbf{r}_{D_1-N_3}$. The differences between the VMC and DMC distributions of $\mathbf{r}_{DN}$ in Fig. 15 are striking. In the DMC distribution we find only two peaks, the largest at approximately 4.5 bohr and a second, slightly broader but less intense at 6.2 bohr. In the VMC simulations we see three peaks. The first two peaks nearly coincide with those in the DMC simulation, but are much less intense, and the dominating feature is at 7.3 bohr. To properly interpret the data in Fig. 15 we measure all the distances between H atoms in molecule i to N atoms in molecule j in the global minimum of the trimer. The distance for a hydrogen bond such as $\mathbf{r}_{D_1-N_2}$, sketched in
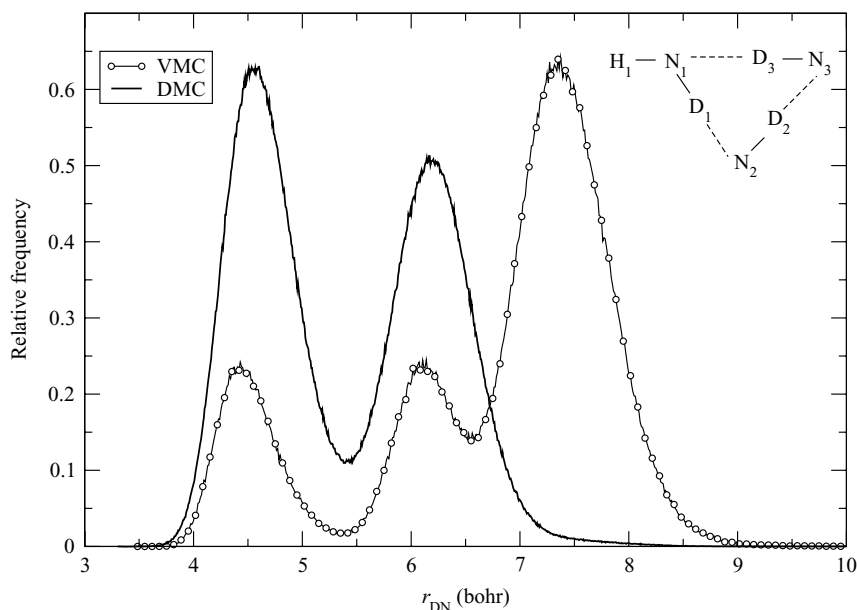
FIG. 15. Histograms of the intermolecular deuterium to nitrogen distance from VMC and DMC simulations of the $(NH_2D)_3$ trimer.

Fig. 15 is 4.34 bohr, the distance such as $\mathbf{r}_{D_1-N_3}$, is 5.99 bohr. Finally, the distance from axial hydrogen atoms (such as H_1) to a neighboring nitrogen atom is either 7.18 or 7.44 bohr. When we consider all six permutations of the molecular labels 1, 2, and 3, we end up with nine values of $\mathbf{r}_{DN}$ at 5.99 bohr and nine values at 4.34 bohr from the global minimum, assuming all three deuterium atoms are on the plane of the molecule and bonded as our sketch suggests. A numerical integration of the heavy dark line in Fig. 15 yields the area of the left peak, from zero to the local minimum at about 5.4 of approximately 0.51, and the area from 5.4 to 10 bohr is 0.49, which is consistent with the statistical weights obtained assuming all thee deuterium atoms are involved in hydrogen bonding. As further evidence, we do not see any peak, or shoulder, near 7.18 or 7.44 bohr in the DMC distribution, whereas a feature at such values is conspicuous in the VMC distributions.

IV. DISCUSSIONS AND CONCLUSIONS

The work presented in this publication has been designed to accomplish several objectives. One main set of goals is to fill in some of the gaps in our knowledge of small ammonia clusters that earlier studies had left behind. In particular, we are interested in determining the exact zero point energy, at least for the smallest clusters, and with it learn about the quantum effects at 0 K on their relative stability and what amount of excess energy is present at low temperatures. This important information can improve our understanding and our ability to predict and explain experimental results, growth patterns in the gas phase and in nanodroplets, and to gauge directly the relative stability as a function of size. With the ground state energy in Table I, we are able to compute the ZPE in the $(NH_3)_{2-5}$ range and note that the ZPE is 42% of the total binding energy of the dimer and drops to 38% for the trimer and to 35% of the total binding energy for the tetramer

and pentamer. Therefore, the quantum effects are substantial at 0 K and the dimer has a relatively small dissociation energy when quantum effects are included. These qualitative observations are in agreement with the path integral results obtained at finite temperatures in our previous work.[7] It is interesting to see that the harmonic estimate is systematically better than the VMC estimate, however, the harmonic analysis we carry out needs hindsight. For the deuterated species, for example, we make sure that the deuterium atoms are in the correct configuration to reflect the true nature of the ground state. Using the DMC energies in Table I we can also determine the relative stability by evaluating the energy differences for the dissociation process at 0 K,

$$(NH_3)_n \longrightarrow (NH_3)_{n-1} + NH_3.$$

The highest dissociation energy is for the tetramer at 6.8 mhartree, making it the most stable of the systems we study here. The dimer at 2.7 mhartree and the pentamer at 4.6 mhartree are the least stable clusters of the group. Furthermore, we observe that there is still a substantial amount of thermal energy present at 40 K in small $(NH_3)_{2-5}$ clusters ranging from 0.2 to 0.6 mhartree in excess of the ground state energy at 40 K.

Characterizing the structure of the ground state wavefunctions is another goal of the present investigation. We discover that the ground state for $n = 3$, 4, and 5 are planar structures in the ground state with the distributions of the molecular centers close to their respective global minima. The dimer, trimer, and the tetramer ground state wavefunctions contain a significant amount of twisted configurations indicating that the wavefunction is spread widely about the degrees of freedom associated with the hydrogen atoms. However, the dimer, trimer, and the tetramer are relatively rigid in those degrees of freedom compared to the high level of fluidity we measure in the pentamer distributions.

With this work we demonstrate that rigid body VMC and DMC simulations using the stereographic projections for molecular clusters are feasible and are hundreds of times more efficient than the equivalent rigid body path integral approach when approaching conditions that favor the ground state. This can be confirmed by comparing the statistical fluctuations of the ground state energy obtained by DMC and the SPPI energy at 4 K for the ND_3 dimer in Table I. As explained earlier, we run rigid-body path integral simulations at the lowest attainable temperatures, mainly, to check that the DMC results are reliable. Despite the technical difficulties we overcome in this work, in particular, the results of the comparisons in Figs. 1 and 6 are reassuring. Nevertheless, while it does give us some confidence to observe the right trend of the energy as the temperature decrease, the agreement between DMC and SPPI is only qualitative. The fact that the difference between the DMC and the SPPI energy at 4 K for the ND_3 dimer is below the statistical noise is in large part the result of the substantial fluctuations in the SPPI estimate, and we speculate that had we been able to attain the same precision at 4 K as we are able with the DMC estimate, we may see a small but significant difference.

Finally, we find the characterization of the ground state wavefunctions of the few isotopomers of the $(NH_3)_{2-5}$ clusters particularly instructive. We present clear evidence that in the dimer and the trimer, the deuterium is preferentially the participating atom in the hydrogen bond. These results are anticipated, in light of experimental and theoretical evidence of the same in water cluster.[64,65] However, it is valuable outcome to confirm the validity of these assumptions with numerical experiments.

ACKNOWLEDGMENTS

[1] T. Kurtn, L. Torpo, C.-G. Ding, H. Vehkamki, M. R. Sundberg, K. Laasonen, and M. Kulmala, J. Geophys. Res. **112**, D04210, doi: 10.1029/2006JD007391 (2007).

[2] P. M. Pawlowski, S. R. Okimoto, and F.-M. Tao, J. Phys. Chem. A **107**, 5327 (2003).

[3] M. Zavka, U.S. Patent 2140254 (1938).

[4] A. W. Hewat and C. Riekel, Acta Crystallogr., Sect. A: Cryst. Phys., Diffr., Theor. Gen. Crystallogr. **35**, 569 (1979).

[5] P. E. Janeiro-Barral and M. Mella, J. Phys. Chem. A **110**, 11244 (2006).

[6] P. E. Janeiro-Barral, M. Mella, and E. Curotto, J. Phys. Chem. A **112**, 2888 (2008).

[7] C. Lubombo, E. Curotto, P. E. Janeiro-Barral, and M. Mella, J. Chem. Phys. **131**, 034312 (2009).

[8] J. A. Odutola, T. R. Dyke, B. J. Howard, and J. S. Muenter, J. Chem. Phys. **70**, 4884 (1979).

[9] D. D. Nelson, Jr., G. T. Fraser, and W. Klemperer, J. Chem. Phys. **83**, 6201 (1985).

[10] D. D. Nelson, Jr., W. Klemperer, G. T. Fraser, F. J. Lovas, and R. D. Suenram, J. Chem. Phys. **87**, 6364 (1987).

[11] S. Süzer and L. Andrews, J. Chem. Phys. **87**, 5131 (1987).

[12] M. Snels, R. Fantoni, R. Sanders, and W. L. Meerts, Chem. Phys. **115**, 79 (1987).

[13] F. Huisken and T. Pertsch, Chem. Phys. **126**, 126 (1988).

[14] M. N. Slipchenko, B. G. Sartakov, and A. F. Vilesov, J. Chem. Phys. **128**, 134509 (2008).

[15] C. Steinbach, U. Buck, and T. A. Beu, J. Chem. Phys. **125**, 133403 (2006).

[16] M. Marchi, M. Sprik, and M. L. Klein, J. Chem. Phys. **89**, 4918 (1988).

[17] S. M. Cybulski, Chem. Phys. Lett. **228**, 451 (1994).

[18] J. S. Lee and S. Y. Park, J. Chem. Phys. **112**, 230 (2000).

[19] J. Stålring, M. Schütz, R. Lindh, G. Karlstrom, and P.-O. Widmark, Mol. Phys. **100**, 3389 (2002).

[20] T. A. Beu and U. Buck, J. Chem. Phys. **114**, 7853 (2001).

[21] T. A. Beu, C. Steinbach, and U. Buck, J. Chem. Phys. **117**, 3149 (2002).

[22] T. A. Beu and U. Buck, J. Chem. Phys. **114**, 7848 (2001).

[23] E. H. T. Olthof, A. van der Avoird, and P. E. S. Wormer, J. Chem. Phys. **101**, 8430 (1994).

[24] K. P. Sagarik, R. Ahlrichs, and S. Brode, Mol. Phys. **57**, 1247 (1986).

[25] A. Hinchliffe, D. G. Bounds, M. L. Klein, I. R. McDonald, and R. Righini, J. Chem. Phys. **74**, 1211 (1981).

[26] G. Duquette, T. H. Ellis, G. Scoles, R. O. Watts, and M. L. Klein, J. Chem. Phys. **68**, 2544 (1978).

[27] R. W. Impey and M. L. Klein, Chem. Phys. Lett. **104**, 579 (1984).

[28] I. R. McDonald and M. L. Klein, J. Chem. Phys. **64**, 4790 (1976).

[29] M. L. Klein, I. R. McDonald, and M. Righini, J. Chem. Phys. **71**, 3673 (1979).

[30] M. F. Russo, Jr. and E. Curotto, J. Chem. Phys. **118**, 6806 (2003).

[31] M. F. Russo, Jr. and E. Curotto, J. Chem. Phys. **120**, 2110 (2004).

[32] M. W. Avilés and E. Curotto, J. Chem. Phys. **122**, 164109 (2005).

[33] E. Curotto, J. Chem. Phys. **123**, 134102 (2005).

[34] S. F. Langley, E. Curotto, D. L. Freeman, and J. D. Doll, J. Chem. Phys. **126**, 084506 (2007).

[35] M. W. Avils and E. Curotto, J. Phys. Chem. A **111**, 2610 (2007).

[36] M. W. Avilés, M. L. McCandless, and E. Curotto, J. Chem. Phys. **128**, 124517 (2008).

[37] M. W. Avilés, P. T. Gray, and E. Curotto, J. Chem. Phys. **124**, 174305 (2006).

[38] E. Curotto, D. L. Freeman, and J. D. Doll, J. Chem. Phys. **128**, 204107 (2008).

[39] T. Luan, E. Curotto, and M. Mella, J. Chem. Phys. **128**, 164102 (2008).

[40] E. Curotto, D. L. Freeman, and J. D. Doll, J. Chem. Phys. **131**, 184508 (2009).

[41] E. Curotto, *Stochastic Simulations of Clusters: Quantum Methods in Flat and Curved Spaces* (Taylor & Francis, London, 2009).

[42] C. Predescu, e-print arXiv:cond-mat/0302171.

[43] C. Predescu, Dubravko Sabo, and J. D. Doll, J. Chem. Phys. **119**, 4641 (2003).

[44] C. Predescu and J. D. Doll, J. Chem. Phys. **117**, 7448 (2002).

[45] C. Predescu, D. Sabo, J. D. Doll, and D. L. Freeman, J. Chem. Phys. **119**, 10475 (2003).

[46] C. Predescu, D. Sabo, J. D. Doll, and D. L. Freeman, J. Chem. Phys. **119**, 12119 (2003).

[47] D. Sabo, C. Predescu, and J. D. Doll, J. Chem. Phys. **121**, 856 (2004).

[48] C. Predescu, P. A. Frantsuzov, and V. A. Mandelshtam, J. Chem. Phys. **122**, 154305 (2005).

[49] R. P. Feynman, Rev. Mod. Phys. **20**, 367 (1948).

[50] L. S. Schulman, *Techniques and Applications of Path Integration* (John Wiley & Sons, New York, 1981).

[51] S. Weinberg, *The Quantum Theory of Fields* (Cambridge University Press, New York, 1996), Vol. 1.

[52] H. Kleinert, *Path integrals in Quantum Mechanics, Statistics and Polymer Physics* (World Scientific, Singapore, 1990).

[53] B. S. DeWitt, Rev. Mod. Phys. **29**, 377 (1957).

[54] E. Curotto, A. Matro, D. L. Freeman, and J. D. Doll, J. Chem. Phys. **108**, 729 (1998).

[55] W. D. Curtis and F. R. Miller, *Differential Manifolds and Theoretical Physics* (Academic, New York, 1985).

[56] M. Falconi and M. W. Deem, J. Chem. Phys. **110**, 1754 (1999).

[57] J. P. Neirotti, F. Calvo, D. L. Freeman, and J. D. Doll, J. Chem. Phys. **112**, 10340 (2000).

[58] F. Calvo, J. P. Neirotti, D. L. Freeman, and J. D. Doll, J. Chem. Phys. **112**, 10350 (2000).

[59] J. P. Neirotti, D. L. Freeman, and J. D. Doll, Phys. Rev. E **62**, 7445 (2000).

[60] M. H. Kalos, D. Levesque, and L. Verlet, Phys. Rev. A **9**, 2178 (1974).

[61] M. H. Kalos and P. A. Whitlock, Monte Carlo Methods (Wiley, New York, 1986).

[62] J. B. Anderson, J. Chem. Phys. **63**, 1499 (1975).

[63] D. M. Ceperley and D. Alder, Science **231**, 555 (1986).

[64] G. T. Fraser, F. J. Lovas, R. D. Suenram, E. N. Karyakin, A. Grushow, W. A. Burns, and K. R. Leopold, J. Mol. Spectrosc. **181**, 229 (1997).

[65] W. Caminati, P. Moreschini, I. Rossi, and P. G. Favero, J. Am. Chem. Soc. **120**, 11144 (1998).